Journal of ELECTRONIC MATERIALS, Vol. 48, No. 11, 2019
https://doi.org/10.1007/s11664-019-07539-2

Bio-assisted Hydrothermal Synthesis and Characterization of $MnWO_4$ Nanorods for High-Performance Supercapacitor Applications

J. YESURAJ,[1,3] E. ELANTHAMILAN,[2] B. MUTHURAAMAN,[1] S. AUSTIN SUTHANTHIRARAJ,[1] and J. PRINCY MERLIN[2]

1.—Department of Energy, University of Madras, Guindy Campus, Chennai 600 025, India. 2.—PG and Research Department of Chemistry, Bishop Heber College, Tiruchirappalli 620 017, India. 3.—e-mail: yesurajjerald@gmail.com

$MnWO_4$ nanorods have been successfully synthesized using a facile, cost-effective DNA-templated hydrothermal method. The effect of the hydrothermal reaction time and DNA template were systematically examined, and both were found to affect the surface morphology of the $MnWO_4$. The prepared specimens were further investigated by x-ray diffraction analysis, Fourier transform-infrared spectroscopy, confocal Raman spectroscopy, high-resolution scanning electron microscopy, and high-resolution transmission electron microscopy. The morphological studies further confirmed formation of $MnWO_4$ nanorod structure (MW-3 specimen) with dimensional size and length of 110 nm and 40 nm, respectively. Electrochemical investigations on the $MnWO_4$ (MW-3 specimen) electrode revealed high specific capacitance of 386 F g^{-1} at scan rate of 5 mV s^{-1} with 90% capacitance retention after 2000 cycles and further excellent rate capability. These findings suggest that such $MnWO_4$ nanorod electrode would be promising candidates for use in energy storage devices.

Key words: $MnWO_4$ nanorods, DNA template, hydrothermal, supercapacitors, energy storage

INTRODUCTION

In recent years, much interest has focused on fabrication of zero- and one-dimensional (1-D) nanostructured inorganic materials due to their electronic, optical, magnetic, and catalytic applications.[1–4] It is well known that the functional properties of nanomaterials mainly depend on their size, shape, morphology, and crystal orientation. Morphology-controlled synthesis of inorganic nanostructures with specific properties is one of the most important issues and main interests in materials science and nanotechnology. In recent years, many synthetic methods have been proposed for preparation of different nanomaterials with particular shapes and morphologies for various applications.[5,6]

Tungstate-based mixed transition-metal oxides (M^{2+} = Co, Cu, Mn, Zn, Fe, Ni) are a class of materials with enhanced performance in various applications.[7–10] Metal tungstates exist in two types of crystal arrangement, namely scheelite and wolframite structures. Bivalent metal cations with larger ionic radius crystallize in scheelite-based structures, while bivalent cations with smaller size can favor formation of Wolframite structures.[11–13] Among them, $MnWO_4$ is a promising candidate because of its distinctive physical and optical properties. Monoclinic manganese tungstate is known as hübnerite, lying in space group *P2/c* and being isostructural with Wolframite-type structure.[14] It is used for various applications including sensors,[15] photocatalysts,[16] magnetic materials,[17] multiferroics,[18] oxidation catalysts, and as supercapacitive[19]

(Received February 28, 2019; accepted August 9, 2019; published online August 22, 2019)

and battery materials.[20] Remarkably, many reports are available on synthesis of $MnWO_4$ nanomaterial with different morphologies. Recently, $MnWO_4$ materials with wire-, flake-, and rice-like morphologies were synthesized by using a DNA-assisted microwave method and were proved to be more suitable for use in magnetic, catalytic, and supercapacitor applications.[19] Hydrothermal and solvothermal methods have also been used to achieve spherical-like structure,[21] nanofibers,[22] nanorods,[23,24] and nanococoons.[25] Thontem et al.[26] prepared a flower-like structure by using a spray pyrolysis method, whereas shuttle-like structures were prepared using a simple precipitation method and investigated for their supercapacitive performance.[27] Most previous reports have mainly focused on synthesis of $MnWO_4$ nanomaterials with various morphologies and their characterization by physiochemical methods.

Both artificial and natural templates are often used as nanoscale templates for synthesis of shape-controlled nanomaterials. Artificial templates such as cetyltrimethylammonium bromide (CTAB), mesoporous carbon, and polymers are frequently used for fabrication of nanostructured materials.[28] On the other hand, Nature provides enormous biomaterials such as DNA,[29] proteins,[30] virus capsids,[31] bacterial cellulose,[32] and globular proteins,[33] which have also been widely used as templates for synthesis of nanoscale materials. They exhibit the capability for self-assembly into a variety of extensive structures with nanoscale dimension. Among the different types of biotemplate, DNA is arguably an excellent biopolymer template for nanoparticle assembly, offering a distinctive programmable nature to tune the shape-controlled properties of nanomaterials. Interestingly, purine, pyrimidine bases, and phosphate groups are present in DNA, which can act as competent chelation sites for orienting the different geometrical forms of nanostructured materials. Several reports are available on such DNA templation in shape-controlled nanomaterials synthesis; For example, Zinchenko et al.[34] prepared spherical-shaped gold nanoparticles through DNA templation for catalytic applications. Woolley and coworkers synthesized copper nanowires using DNA as a template.[29] The Kundu group synthesized CoS–DNA molecular hybrids for electrocatalytic applications.[35] Li et al. reported preparation of nickel cobalt oxide nanoflakes via a DNA template method and their use for supercapacitor electrode applications. Other reports are also available on preparation of Pd,[36] Pt,[37] Cu,[29] PbS,[38] TiO_2,[39] Fe_3O_4,[40] Ni,[41] and Bi_2S_3[42] nanoparticles using DNA as a template.

We report herein the synthesis of $MnWO_4$ nanorods via a simple, cost-effective DNA-templated hydrothermal method and an investigation of its structural, morphological, and electrochemical properties. The electrochemical properties of the as-prepared $MnWO_4$ were evaluated by means of cyclic voltammetry, galvanostatic charge/discharge measurements, electrochemical impedance spectroscopy (EIS), and cycling stability measurements, revealing excellent double-layer capacitance characteristics as well as high specific capacitance, rate capability, and capacitance retention. The results obviously demonstrate that thus-prepared $MnWO_4$ nanorods are potential candidates for fabrication of energy storage devices.

EXPERIMENTAL PROCEDURES

Materials

All chemicals and reagents employed were of analytical grade and used without further purification. Sodium tungstate dihydrate ($Na_2WO_4{\cdot}2H_2O$), ethanol, and *N*-methyl-2-pyrrolidone (NMP) were acquired from SRL (India). On the other hand, manganese acetate tetrahydrate ($MnC_2H_6O_4{\cdot}4H_2O$), deoxyribonucleic acid (DNA) sodium salt from herring testes, polyvinylidene fluoride (PVDF), and carbon black were purchased from Sigma Aldrich. In addition, nickel foil (0.025 mm thickness) was obtained directly from Alfa Aesar. Deionized (DI) water was used in all synthesis procedures and other studies.

Synthesis of $MnWO_4$ Nanomaterials

In a typical synthesis, aqueous solution of DNA was prepared by dissolving 0.003 g deoxyribonucleic acid (DNA) sodium salt in 50 mL DI water with further stirring for 12 h using a magnetic stirrer to obtain a homogeneous solution. Subsequently, 50 mM (0.858 g) manganese acetate tetrahydrate ($MnC_2H_6O_4{\cdot}4H_2O$) and 50 mM (1.15 g) sodium tungstate dihydrate ($Na_2WO_4{\cdot}2H_2O$) were dissolved in 20 mL DI water in separate beakers under constant stirring. Thereafter, 50 mL DNA aqueous solution was gradually added to the manganese precursor. Subsequently, the two aforementioned precursors were mixed together by constant stirring and transferred to a 100-mL autoclave. After sealing, it was heated to 180°C for 6 h and naturally cooled to room temperature. The resultant precipitate was washed several times using ethanol and DI water to remove all impurities. The precipitate obtained was dried in a hot air oven at 80°C for 12 h and later at 500°C for 3 h. For comparison, control experiments were also performed at 12 h and 24 h intervals. The materials synthesized using hydrothermal preparation for 6 h, 12 h, and 24 h were named MW-1, MW-2, and MW-3, respectively.

Characterization

The crystal structure of the synthesized samples was studied by x-ray diffraction (XRD) analysis using a PANalytical X'PertPRO diffractometer with Cu K_α radiation (λ = 0.154060 nm). Fourier-transform infrared (FTIR) spectra were recorded in the range from 4000 cm^{-1} to 400 cm^{-1} using a

PerkinElmer RX1 spectrophotometer. Raman spectra of all the prepared specimens were collected in the range from 2000 cm^{-1} to 250 cm^{-1} using a I-11 confocal Raman spectrophotometer (Nanophoton Corp., Japan). The surface morphology of the prepared $MnWO_4$ samples was analyzed by high-resolution scanning electron microscopy (HR-SEM, FEI Quanta FEG 200) and transmission electron microscope (HR-TEM, Tecnai G2S-TWIN, FEI, 200 kV) system.

Electrochemical Characterization

The electrochemical performance of the prepared $MnWO_4$ nanorods was explored using a three-electrode system on a Bio-Logic electrochemical workstation (model VSP-150) with aqueous 1 M Na_2SO_4 as electrolyte. The working electrode was prepared by mixing of the sample under study, acetylene black and Polyvinylidene fluoride (PVDF) in a mass ratio of 80:10:10. The hybrid material was mixed with *N*-methyl-2-pyrrolidone as solvent, and the resultant homogeneous slurry was coated on nickel foil. The as-prepared working electrode was dried in a vacuum oven at 80°C for 12 h. The weight of active material in the as-prepared electrode was 5 mg. Platinum wire and saturated calomel electrode (SCE) were used as counter and reference electrode, respectively. The supercapacitive performance of the electrodes was evaluated by cyclic voltammetry (CV) and galvanostatic charge/discharge measurements at various rates. The specific capacitance of the supercapacitor electrode was calculated by CV and galvanostatic charge/discharge measurements using Eq. 1 and 2, respectively:[43]

$$C_{sp} = \frac{\int i dV}{S \cdot \Delta V \cdot m}, \quad (1)$$

$$C_{sp} = \frac{I \Delta t}{m \Delta V}, \quad (2)$$

where $\int i dV$ denotes the integral area of the CV curve, ΔV is the potential window (V), m is the mass of active material (mg), S is the scan rate (mV s^{-1}). I is the discharge current density (A), and Δt is the discharge time (s).

RESULTS AND DISCUSSION

The freshly synthesized $MnWO_4$ nanomaterial specimens MW-1, MW-2, and MW-3 were characterized by powder XRD analysis to determine their phase and purity (Fig. 1). The observed diffraction peaks located at 2θ = 23.5°, 24.0°, 29.8°, 30.2°, 31.0°, 35.9°, 36.2°, 37.2°, 40.2°, 40.4°, 40.8°, 40.9°, 43.3°, 44.0°, 44.8°, 47.2°, 48.1°, 49.2°, 51.1°, 52.1°, 53.0°, 53.2°, 54.4°, 55.7°, 57.5°, 59.6°, 60.5°, 61.3°, 62.3°, 63.1°, 64.5°, 67.6°, 69.2°, 70.8°, 73.2°, 76.2°, and 77.3° could be perfectly indexed to the (011), (110), (−111), (111), (020), (002), (120), (200), (−102),

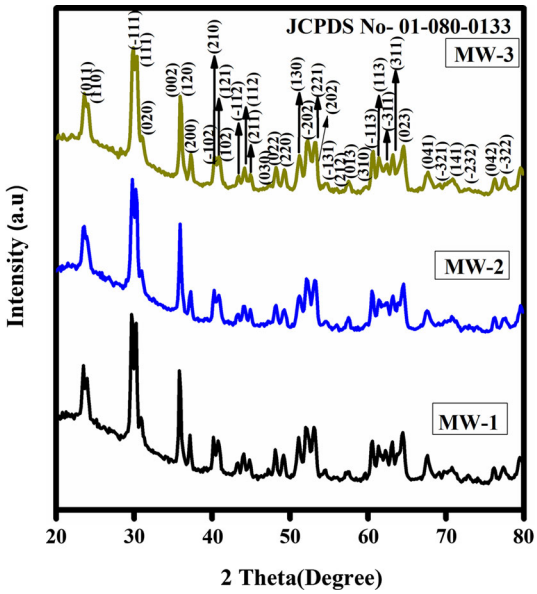

Fig. 1. XRD patterns of synthesized $MnWO_4$ specimens MW-1, MW-2, and MW-3.

(210), (121), (102), (−112), (112), (211) (030), (022), (220), (130), (−202), (221), (202), (−131), (212), (013), (310), (−113), (113), (−311), (311), (023), (041), (−321), (141), (−232), (042), and (−322) planes of monoclinic $MnWO_4$ material in Joint Committee on Powder Diffraction Standards (JCPDS) card no. 01-080-0133 and space group *P2/C*. Noticeably, no other impurity peaks were observed, suggesting a high purity for these $MnWO_4$ specimens. The Scherrer formula was used to calculate the average crystallite size of the prepared $MnWO_4$ specimens:

$$D = \frac{0.9\lambda}{\beta \cos\theta}, \quad (3)$$

where λ, β, and θ are the x-ray wavelength, full-width at half-maximum, and diffraction angle, respectively. The average crystallite size of the MW-1, MW-2, and MW-3 specimens was found to be 12.2 nm, 13.5 nm, and 14.9 nm, respectively.

FTIR spectroscopy is commonly used to evaluate the nature of bonding and functional properties of compounds. Figure 2 shows the FTIR spectrum of $MnWO_4$ nanomaterial prepared via DNA-templated synthesis with the features labeled. All the bands observed at 882 cm^{-1}, 820 cm^{-1}, 722 cm^{-1}, 587 cm^{-1}, 520 cm^{-1}, 455 cm^{-1}, and 422 cm^{-1} correspond to characteristic peaks of $MnWO_4$ material. The pair of bands at 882 cm^{-1} and 820 cm^{-1} correspond to symmetric and asymmetric stretching vibration modes of the short W–O bond in terminal WO_2 groups. The bands seen at 722 cm^{-1} and 587 cm^{-1} may be associated with the asymmetrical stretching vibrations (B_u and A_u) of the longer W–O bond in the $(W_2O_4)_n$ chain, while the typical bands

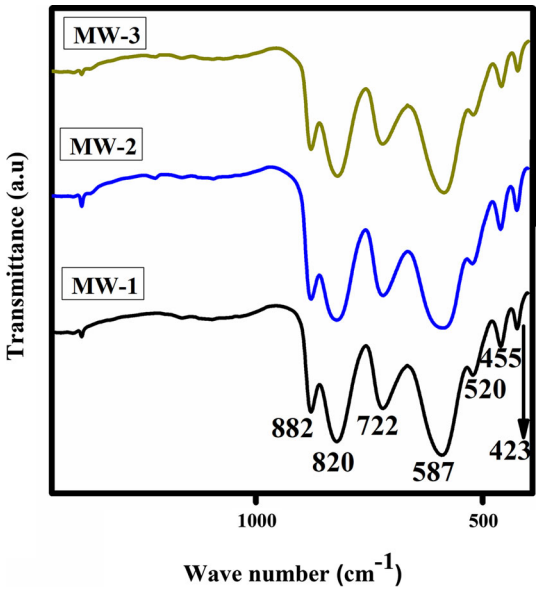

Fig. 2. FTIR spectra of synthesized $MnWO_4$ specimens MW-1, MW-2, and MW-3.

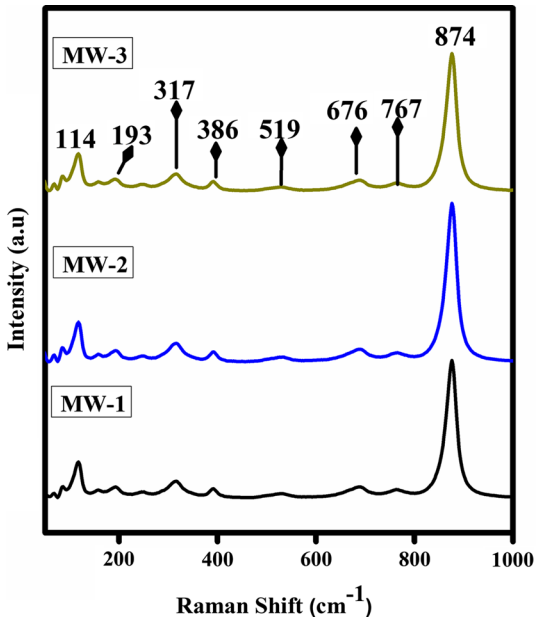

Fig. 3. Confocal Raman spectra of synthesized $MnWO_4$ specimens MW-1, MW-2, and MW-3.

at 520 cm^{-1} and 455 cm^{-1} are assigned to the in-plane deformation modes (A_u and B_u) of the longer W–O bond. The particular band at 422 cm^{-1} may be ascribed to the in-plane deformation vibration (B_u) of W–O bond in terminal WO_2 groups,[21,44,45] as further confirmed by confocal Raman spectroscopic analysis.

The confocal Raman spectra obtained for the synthesized $MnWO_4$ materials MW-1, MW-2, and MW-3 are displayed in Fig. 3. Eight modes were obtained in the range of 100 cm^{-1} to 1000 cm^{-1} at room temperature. The spectra displayed one prominent high-intensity peak at 874 cm^{-1}, corresponding to symmetric stretching vibration (A_g) of the short terminal W–O bond. The band at 767 cm^{-1} is attributed to asymmetric stretching vibration (B_g) of the short terminal W–O bond. The symmetric (A_g) and asymmetric stretching vibration (B_g) modes of longer W–O bonds in $(W_2O_4)_n$ chains are found to appear at 517 cm^{-1} and 676 cm^{-1}, respectively. The peaks at 386 cm^{-1} and 317 cm^{-1} can be ascribed to the deformation vibration (A_g) of short W–O bond and vibration modes of Mn–O, respectively. The remaining two peaks at 193 cm^{-1} and 114 cm^{-1} originate from interchain deformation modes and lattice modes.[11,15,21,44,46] These XRD, Raman, and FTIR results thus confirm formation of high-purity $MnWO_4$ specimens.

The surface morphology of the $MnWO_4$ specimens prepared via DNA-mediated hydrothermal synthesis was characterized using high-resolution scanning electron microscopy (HR-SEM) and high-resolution transmission electron microscopy (HR-TEM). HR-SEM images of $MnWO_4$ specimens MW-1, MW-2, and MW-3 are shown in Fig. 4a–f, clearly revealed the effect of DNA mediation and hydrothermal reaction time on the morphology of the freshly prepared specimens. The morphological images of specimen MW-1 clearly exhibit a mixed structure containing both edge-curved nanorods and nanoparticles (38 nm in size), assembled together to form an aggregated morphology (Fig. 4a, b). Figure 4c and d correspond to specimen MW-2 and clearly show that there was no particular change in morphology when the hydrothermal reaction time was increased from 6 h to 12 h, whereas the number of nanoparticles decreased. Interestingly, only perfect nanorod morphology with length and size of 110 nm and 40 nm, respectively, was obtained in the case of MW-3 specimen, as shown in Fig. 4e, f. The nanorods were found to be edge curved, which is highly beneficial for electrochemical supercapacitive performance. These results clearly indicate a transition of the nanorods from mixed morphology with nanoparticles depending on the DNA mediation and increased hydrothermal reaction time. The strategy for DNA-templated hydrothermal synthesis of $MnWO_4$ nanorods as reported in literature[47] is illustrated in Scheme 1.

The structural details of the nanorods obtained in specimen MW-3 were further investigated by HR-TEM analysis (Fig. 5). A morphology resembling uniform nanorods was also evident from the HR-TEM image obtained for specimen MW-3, in good agreement with the HR-SEM results presented in Fig. 5a, and b. Furthermore, Figs. S1 and S2 (Electronic Supplementary Material) show lower- and higher-magnification images of specimen MW-3,

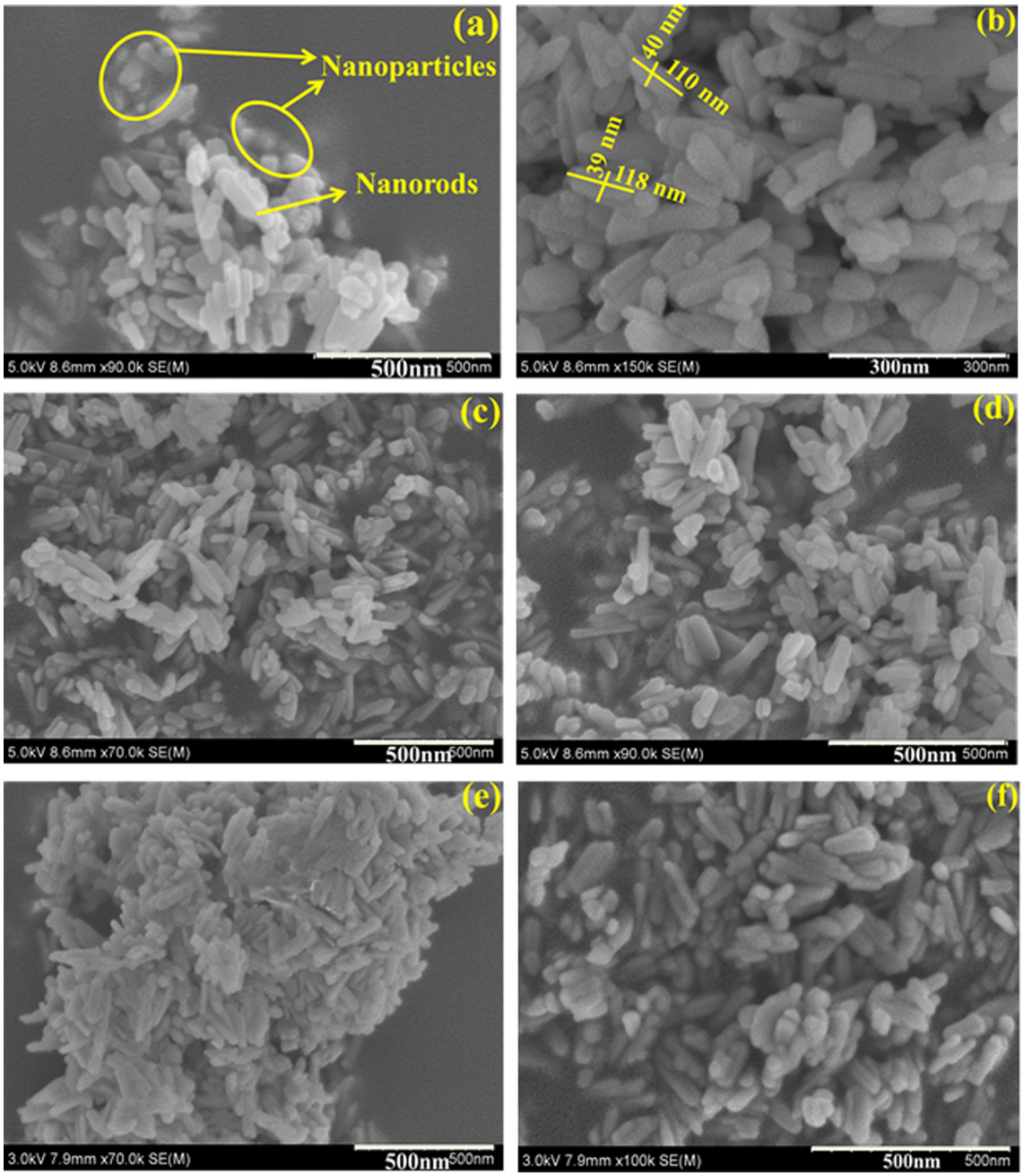

Fig. 4. HR-SEM micrographs of synthesized $MnWO_4$ specimens (a, b) MW-1, (c, d) MW-2, and (e, f) MW-3.

revealing homogeneously formed edge-curved nanorods. Additionally, a sole edge-curved nanorod is also shown in Fig. S3 (supplementary information). Moreover, small pores are perfectly visible over the surface of the edge-curved nanorods. Figure 5c and d provides additional crystal structure information in the case of specimen MW-3. HR-TEM analysis of an individual nanorod (Fig. 5c) revealed clear lattice fringes with primary interplanar distances of 0.37 nm and 0.29 nm, which can be assigned to the (011) and (−111) crystallographic planes. The selected-area electron diffraction (SAED) pattern recorded for a single nanorod in MW-3 specimen is depicted in Fig. 5d, revealing its perfect crystalline nature. The results observed in terms of lattice fringes and SAED pattern are in good agreement with the XRD data too.

Electrochemical Analysis

To evaluate the features of the prepared unique $MnWO_4$ nanostructures as electrochemical supercapacitive electrodes, electrochemical measurements such as cyclic voltammetry (CV),

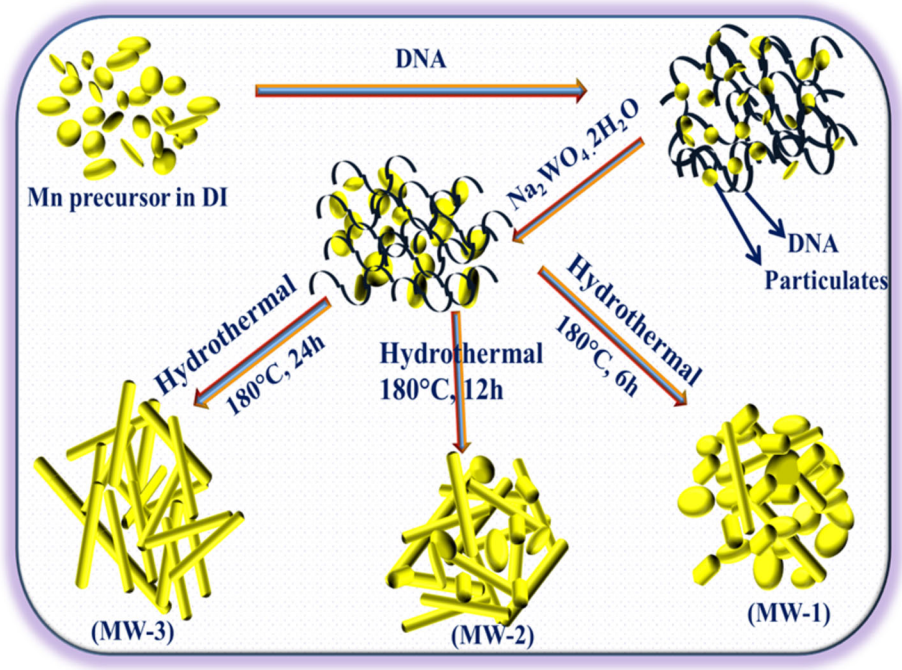

Scheme 1. Pictorial representation for the preparation of $MnWO_4$ materials.

chronopotentiometry (CP), and cycling stability studies were performed in a three-electrode system using aqueous 1 M Na_2SO_4 as electrolyte solution. Cyclic voltammetry is a well-known method used to determine the specific capacitance of any given material. Figure 6a, b, and c display the CV curves obtained for specimens MW-1, MW-2, and MW-3 in the potential range from 0 V to 1 V at scan rates of 5 mV s^{-1} to 100 mV s^{-1}. Remarkably, the CV curves of the freshly prepared $MnWO_4$ electrode materials displayed a distinct rectangular shape at different scan rates, with no obvious peaks for oxidation and reduction reactions, which tends to indicate an electric double-layer charge storage mechanism.[48] Fascinatingly, the fact that the current density increased with increasing scan rate further confirms the superior capacitive behavior of the $MnWO_4$ electrodes. Moreover, the shape of the CV curve remained the same at the highest scan rate of 100 mV s^{-1}, demonstrating a superior rate capability, mass transportation, and excellent frequency response.[49] The area under the CV curve of the $MnWO_4$ electrode materials increased at higher scan rate, which may be due to fast transportation of ions from the aqueous electrolyte solution towards the electrode–electrolyte interface.[50] The specific capacitance of the different $MnWO_4$ electrodes can be calculated from CV curves using Eq. 2. The observed specific capacitance values of the MW-1, MW-2, and MW-3 electrodes were found to be 181 F g^{-1}, 350 F g^{-1}, and 386 F g^{-1} at 5 mV s^{-1}. Overall, specimen MW-3 tended to exhibit higher specific capacitance at given scan rate, indicating its pronounced supercapacitive performance. Comparing the capacitive performance of electrode MW-3 with other reported $MnWO_4$-based electrode materials, it is clearly observed that the specific capacitance of the as-prepared $MnWO_4$ electrode in the present study is higher than that of reported $MnWO_4$-, Mn-, and W-based nanostructures (Table I). This further demonstrates the improved pseudocapacitive performance of the freshly prepared $MnWO_4$ electrode materials.

Furthermore, on increasing the scan rate to 100 mV s^{-1}, the MW-1, MW-2, and MW-3 electrode materials still delivered capacitance of 124 F g^{-1}, 245 F g^{-1}, and 288 F g^{-1}, respectively, confirming their good rate capability at higher scan rates. The effect of the scan rate on the specific capacitance is further displayed in Fig. 6d. On increasing the scan rate from 5 mV s^{-1} to 100 mV s^{-1}, the specific capacitance decreased due to restricted diffusion of electrolyte ions on the surface.[59]

To further evaluate the electrochemical supercapacitive performance of the prepared $MnWO_4$ materials (MW-1, MW-2, and MW-3 electrodes), galvanostatic charge/discharge analysis was performed in the potential window from 0 V to 1 V at five different current densities of 1 A g^{-1}, 1.5 A g^{-1}, 2 A g^{-1}, 2.5 A g^{-1}, and 3 A g^{-1} (Fig. 7a–c). It is interesting to note that the $MnWO_4$ electrodes exhibited a triangular charge–discharge profile, further confirming the operation of an electric double-layer mechanism and indicating their good capacitive property as well as reversibility.[60] Besides, the absence of *IR* drops for all the prepared electrode materials can be ascribed to their low internal resistance and the good contact between

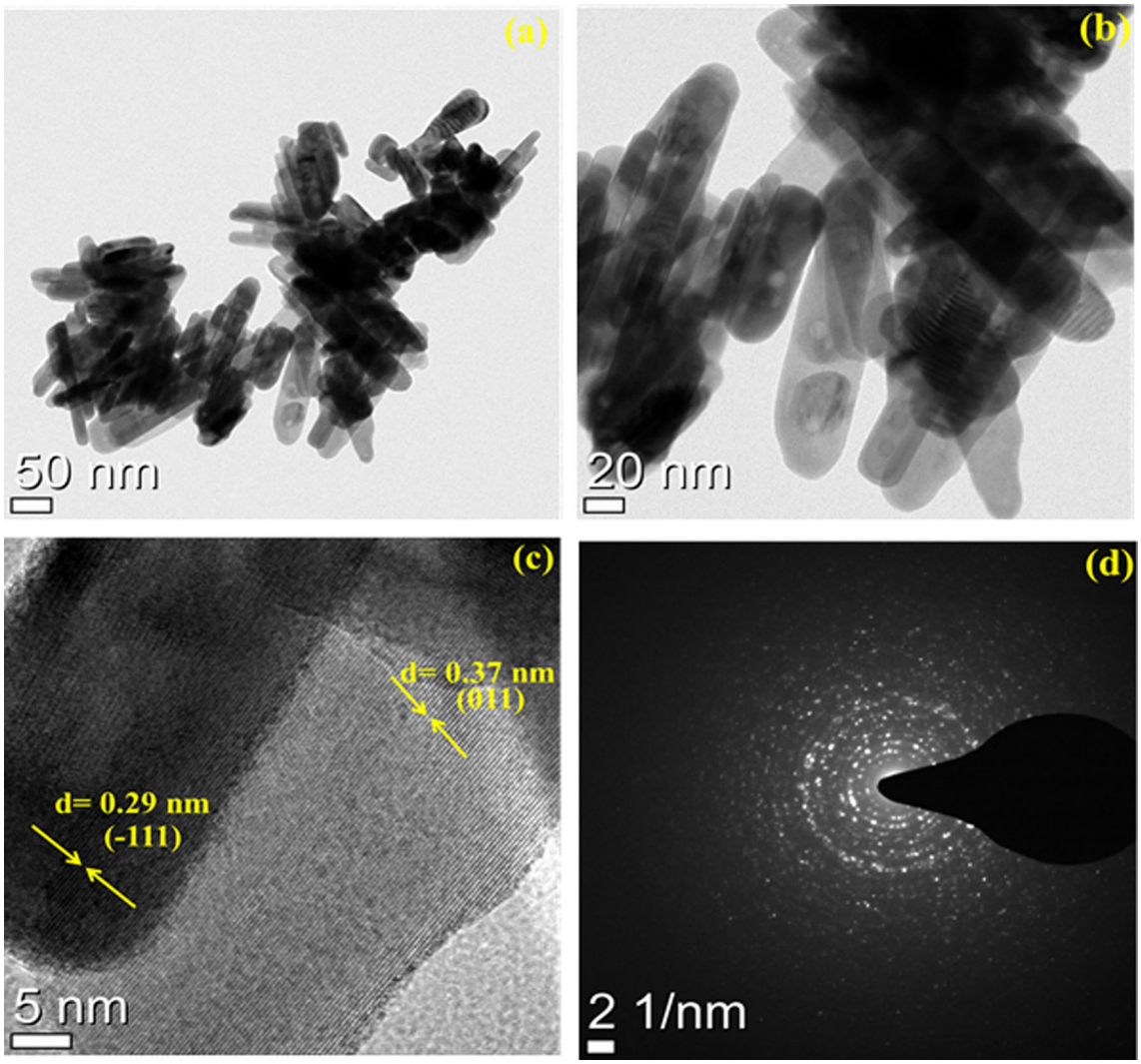

Fig. 5. (a, b) HR-TEM images and (c, d) lattice fringes and SAED patterns of specimen MW-3.

the active electrode materials and current collector.[61] The specific capacitance values calculated from the galvanostatic charge–discharge curves using Eq. 3 were found to be 87 F g^{-1}, 146 F g^{-1}, and 243 F g^{-1} for electrodes MW-1, MW-2, and MW-3, respectively, at current density of 1 A g^{-1}. Comparatively, electrode MW-3 exhibited high specific capacitance according to both the CV and CP analyses, which might be due to the following reasons: (1) the presence of active redox sites in the $MnWO_4$ nanorods enhances the specific capacitance value, (2) the small $MnWO_4$ nanorods obtained in MW-3 specimen would efficiently reduce the ion diffusion path length for enhanced ion transportation,[62] and (3) the synergistic effect between $MnWO_4$ nanorods. The estimated specific capacitance values are plotted against current density in Fig. 7d, showing agreement with the CV results. These features are predominantly favorable for real-time supercapacitor applications.

Electrochemical impedance spectroscopy (EIS) was carried out to further examine the capacitive properties of the $MnWO_4$ materials. The Nyquist and enlarged Nyquist plots (inset) of the materials are displayed in Fig. 8. All materials exhibited similar shapes of Nyquist curves, with each EIS curve showing a short arc in the high frequency region followed by a nearly vertical line in the low frequency region.[63,64] The diameter of the arc corresponds to the charge transfer resistance, while the nearly vertical line is related to the capacitive behavior.[65] It is interesting to note that the charge transfer resistance (R_{ct}) of the MW-3 electrode was lower compared with those of the MW-1 and MW-2 electrodes, revealing the good capacitance behavior of the MW-3 electrode material. Furthermore, the

Table I. Comparison of electrochemical performance of different electrode materials

Material	Electrolyte	Specific Capacitance (F g^{-1})	Ref.
$MnWO_4$	0.1 M Na_2SO_4	34	19
$MnWO_4$	1 M KOH	295	27
$MnWO_4$	1 M H_2SO_4	27	51
$MnWO_4$/reduced graphene	6 M KOH	288	52
MnO_2-based mixed oxides	1 M Na_2SO_4	210	53
MnO_2	0.1 M Na_2SO_4	250	54
ε-MnO_2	1 M Na_2SO_4	123	55
WO_3–WO_3·0.5H_2O	0.5 M H_2SO_4	290	56
WO_3	1 M Na_2SO_4	266	57
WO_3	0.5 M H_2SO_4	319.26	58
$MnWO_4$	1 M Na_2SO_4	386	Present

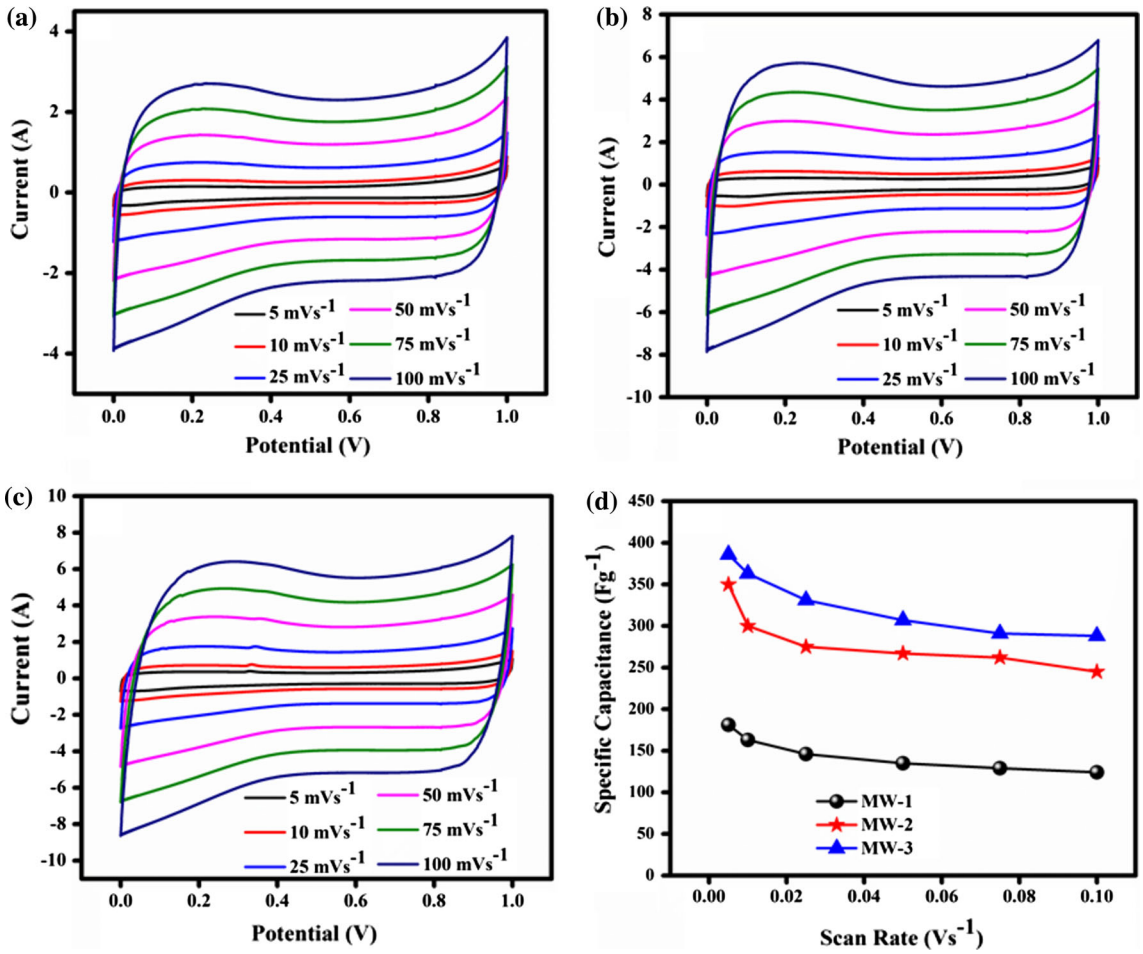

Fig. 6. Cyclic voltammetry curves of $MnWO_4$ specimens at different scan rates in three-electrode system: (a) MW-1, (b) MW-2, and (c) MW-3; (d) variation of specific capacitance of $MnWO_4$ specimens versus scan rate.

point of intersection of the EIS curve with the real axis in the high frequency region indicates the surface resistance (R_s).[66] The surface resistance is a combination of the ionic resistance of the electrolyte, the intrinsic resistance of the active electrode material, and the contact resistance at the active material–current collector interface.[67] The surface resistance of the MW-3 electrode was lower than those of the other electrodes (MW-1 and MW-2). This result proves that the MW-3 electrode offered greatly improved capacitance due to its perfect nanorod structure, which is well consistent with the cyclic voltammetry and galvanostatic charge–discharge results.

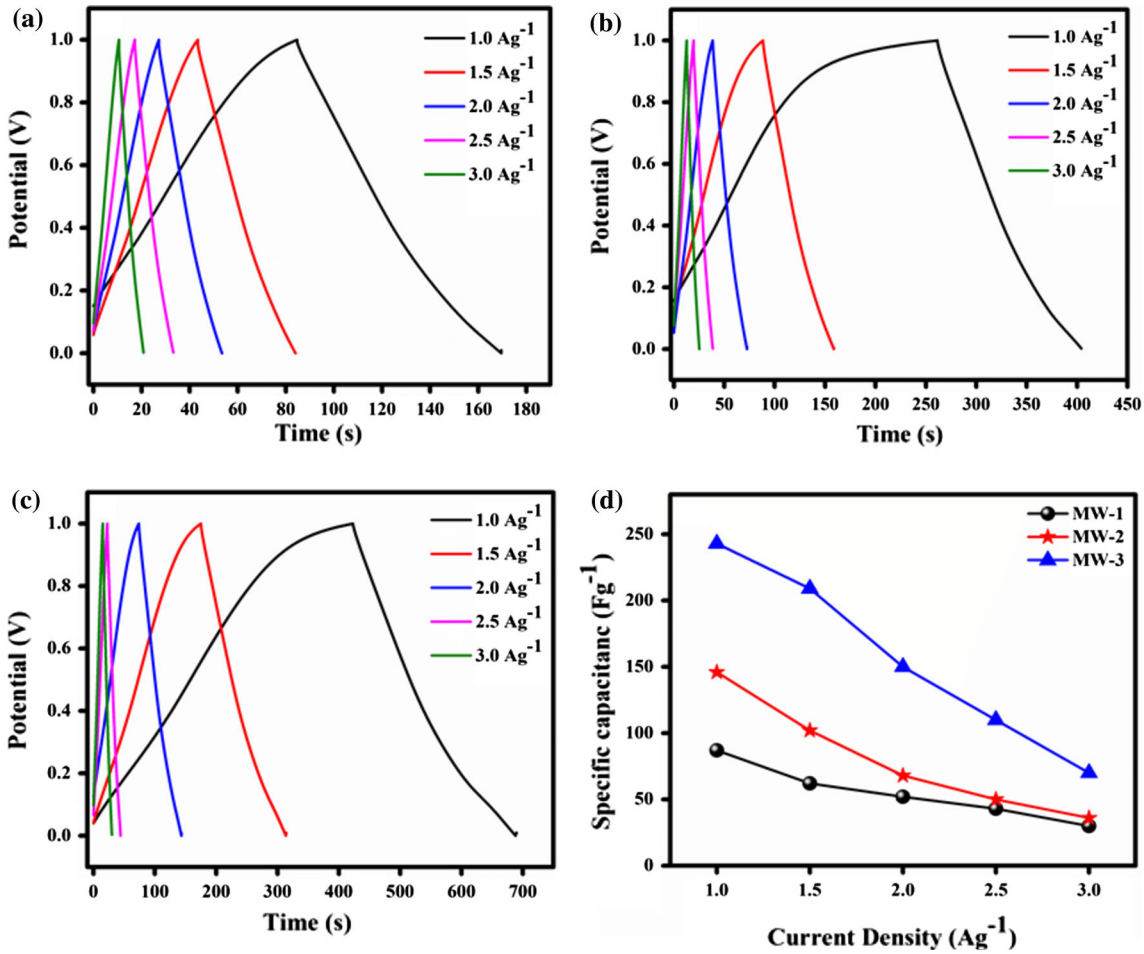

Fig. 7. Galvanostatic charge–discharge curves of $MnWO_4$ specimens (a) MW-1, (b) MW-2, and (c) MW-3; (d) variation of specific capacitance of $MnWO_4$ specimens versus current density.

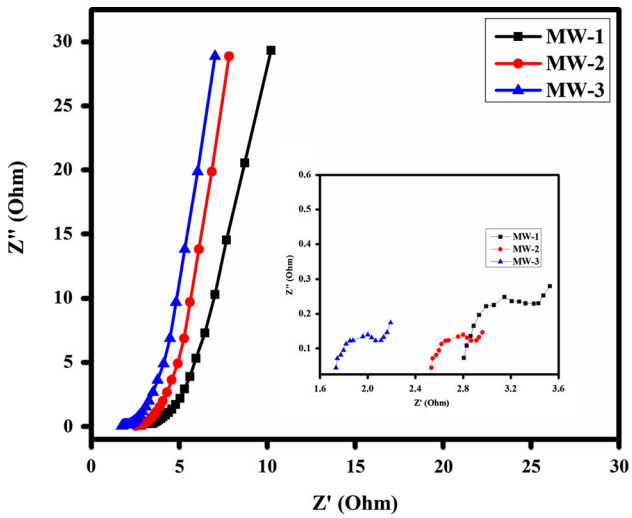

Fig. 8. Electrochemical impedance spectroscopy of samples MW-1, MW-2, and MW-3 with enlarged Nyquist plots inset.

Achievement of a long cycling stability window is an additional criterion determining the scope of real-time supercapacitor applications. To estimate the cycling stability, all the prepared $MnWO_4$ electrodes were evaluated at a higher scan rate of 100 mV s^{-1} in the potential range between 0 V and 1 V for 2000 cycles in aqueous 1 M Na_2SO_4 (Fig. 9). In the first 400 cycles for all three electrodes, the specific capacitance increased with cycles, which can be attributed to electrochemical activation of the prepared $MnWO_4$ specimens.[68] Subsequently, the capacitance values gradually decreased with cycle number then remained stable until 2000 cycles. The MW-3 electrode exhibited outstanding long-term stability with only 10% capacitance loss even after 2000 cycles, which is evidently much better than the 21% and 16% capacitance loss noticed for electrodes MW-1 and MW-2 after the same number of cycles. The inset of Fig. 9 shows the cycling stability results at the 1st and 2000th cycles for specimen MW-3. On the other hand, Fig. S4

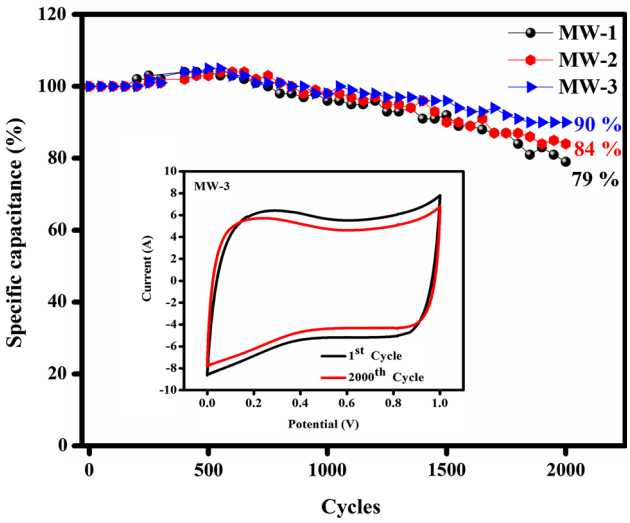

Fig. 9. Cyclic performance of $MnWO_4$ specimens at scan rate of 100 mV s^{-1} using three-electrode system; Inset: 1st and 2000th cycles of specimen MW-3.

(Electronic Supplementary Material) shows the stability results at the 1st and 2000th cycles for electrodes MW-1 and MW-2. Comparatively, specimen MW-3 exhibited excellent electrochemical performance including higher specific capacitance, good rate capability, and excellent long-term stability. The results of this work confirm the potential of such $MnWO_4$ nanorods (specimen MW-3) for application in next-generation high-performance electrochemical supercapacitive energy storage devices.

CONCLUSIONS

$MnWO_4$ nanorods were successfully synthesized by a facile, cost-effective DNA-templated hydrothermal technique and their supercapacitive performance investigated in a three-electrode configuration. Furthermore, the physicochemical properties of the as-prepared $MnWO_4$ specimens were systematically analyzed using various characterization techniques. The electrode formed from specimen MW-3 showed enhanced specific capacitance of 386 F g^{-1} at scan rate of 5 mV s^{-1} with 90% capacitance retention after 2000 cycles at scan rate of 100 mV s^{-1} and excellent rate capability. These excellent electrochemical properties of the $MnWO_4$ nanorod electrode make it a potential candidate for use in supercapacitor applications.

ELECTRONIC SUPPLEMENTARY MATERIAL

HR-TEM images of specimen MW-3 and 1st and 2000th cycle stability results of MW-1 and MW-2 electrodes.

ACKNOWLEDGMENTS

This work was supported by the DST-PURSE PHASE-II Program from Department of Science and Technology (DST), Government of India, New Delhi. J.Y. gratefully acknowledges the University of Madras for the award of a University Research Fellowship (URF).

ELECTRONIC SUPPLEMENTARY MATERIAL

The online version of this article (https://doi.org/10.1007/s11664-019-07539-2) contains supplementary material, which is available to authorized users.

REFERENCES

1. L.S. Kumari, P. Prabhakar Rao, S. Sameera, V. James, and P. Koshy, *Mater. Res. Bull.* 70, 93 (2015).
2. Q. Song and Z.J. Zhang, *J. Am. Chem. Soc.* 126, 6164 (2004).
3. R. Narayanan and M.A. El-Sayed, *Nano Lett.* 4, 343 (2004).
4. C. Ji, F. Liu, L. Xu, and S. Yang, *J. Mater. Chem. A* 5, 5568 (2017).
5. S.R. Ede and S. Kundu, *ACS Sustain. Chem. Eng.* 3, 2321 (2015).
6. W.B. Hu, X.L. Nie, and Y.Z. Mi, *Mater. Charact.* 61, 85 (2009).
7. S. Mahdi, M. Rahimi-Nasrabadi, and M. Khalilian-Shalamzari, *Appl. Surf. Sci.* 263, 745 (2012).
8. X. Xing, Y. Gui, G. Zhang, and C. Song, *Electrochim. Acta* 157, 15 (2015).
9. Y. Su, B. Zhu, K. Guan, S. Gao, L. Lv, C. Du, L. Peng, and L. Hou, *J. Phys. Chem. C* 116, 18508 (2012).
10. Y. Zhou, H. Yao, Q. Zhang, J. Gong, S. Liu, and S. Yu, *Society* 48, 1082 (2009).
11. L.H. Hoang, N.T.M. Hien, W.S. Choi, Y.S. Lee, K. Taniguchi, T. Arima, S. Yoon, X.B. Chena, and I.S. Yang, *J. Raman Spectrosc.* 41, 1005 (2010).
12. S.M.M. Zawawi, R. Yahya, A. Hassan, H.N.M.E. Mahmud, and M.N. Daud, *Chem. Cent. J.* 7, 80 (2013).
13. H.-W. Shim, I.-S. Cho, K.S. Hong, A.-H. Lim, and D.-W. Kim, *J. Phys. Chem. C* 115, 16228 (2011).
14. H.W. Shim, A.H. Lim, J.C. Kim, G.H. Lee, and D.W. Kim, *Chem. Asian J.* 8, 2851 (2013).
15. S. Muthamizh, R. Suresh, K. Giribabu, R. Manigandan, S. Praveen Kumar, S. Munusamy, and V. Narayanan, *J. Alloys Compd.* 619, 601 (2015).
16. M. Vosoughifar, *J. Mater. Sci. Mater. Electron.* 28, 2135 (2017).
17. J. Ungelenk, S. Roming, P. Adler, W. Schnelle, J. Winterlik, C. Felser, and C. Feldmann, *Solid State Sci.* 46, 89 (2015).
18. H. Zhou, Y. Yiu, M.C. Aronson, and S.S. Wong, *J. Solid State Chem.* 181, 1539 (2008).
19. U. Nithiyanantham, S.R. Ede, T. Kesavan, P. Ragupathy, M.D. Mukadam, S.M. Yusuf, and S. Kundu, *RSC Adv.* 4, 38169 (2014).
20. E. Zhang, Z. Xing, J. Wang, Z. Ju, and Y. Qian, *RSC Adv.* 2, 6748 (2012).
21. W. Tong, L. Li, W. Hu, T. Yan, X. Guan, and G. Li, *J. Phys. Chem. C* 114, 15298 (2010).
22. S. Lei, K. Tang, Z. Fang, Y. Huang, and H. Zheng, *Nanotechnology* 16, 2407 (2005).
23. M.A.P. Almeida, L.S. Cavalcante, M.S. Li, J.A. Varela, and E. Longo, *J. Inorg. Organomet. Polym Mater.* 22, 264 (2012).

24. S.-J. Chen, X.-T. Chen, Z. Xue, J.-H. Zhou, J. Li, J.-M. Hong, and X.-Z. You, *J. Mater. Chem.* 13, 1132 (2003).
25. W.B. Hu, X.L. Nie, and Y.Z. Mi, *Mater. Charact.* 61, 85 (2010).
26. S. Thongtem, S. Wannapop, and T. Thongtem, *Trans. Nonferrous Met. Soc. China* 19, S100 (2009).
27. F. Li, X. Xu, J. Huo, and W. Wang, *Mater. Chem. Phys.* 167, 22 (2015).
28. Y. Xie, D. Kocaefe, C. Chen, and Y. Kocaefe, *J. Nanomater.* 2016, 1 (2016).
29. C.F. Monson and A.T. Woolley, *Nano Lett.* 3, 359 (2003).
30. U.B. Sleytr, P. Messner, D. Pum, and M. Sára, *Angew. Chemie Int. Ed.* 38, 1034 (1999).
31. B.Y. Huang, A. Yu, C. Huang, L. Gan, X. Zhao, Y. Lin, B. Zhang, and T. Tbl, **4095**, 627 (1999).
32. S. Ifuku, M. Tsuji, M. Morimoto, H. Saimoto, and H. Yano, *Biomacromol* 10, 2714 (2009).
33. I. Yamashita, *Thin Solid Films* 393, 12 (2001).
34. A. Zinchenko, Y. Miwa, L.I. Lopatina, V.G. Sergeyev, S. Murata, and A.C.S. Appl, *Mater. Interfaces* 6, 3226 (2014).
35. S.R. Ede, S. Kundu, and A.C.S. Sustain, *Chem. Eng.* 3, 2321 (2015).
36. C. Fang, Y. Fan, J.M. Kong, G.J. Zhang, L. Linn, and S. Rafeah, *Sensors Actuators B Chem.* 126, 684 (2007).
37. R. Seidel, L.C. Ciacchi, M. Weigel, W. Pompe, and M. Mertig, *J. Phys. Chem. B* 108, 10801 (2004).
38. J. Su and F. Gao, *Mater. Lett.* 108, 58 (2013).
39. U. Nithiyanantham, A. Ramadoss, S.R. Ede, and S. Kundu, *Nanoscale* 6, 8010 (2014).
40. D. Nyamjav and A. Ivanisevic, *Biomaterials* 26, 2749 (2005).
41. Q. Gu, C. Cheng, S. Suryanarayanan, K. Dai, and D.T. Haynie, *Phys. E Low Dimens. Syst. Nanostruct.* 33, 92 (2006).
42. Q. Lu, F. Gao, and S. Komarneni, *J. Am. Chem. Soc.* 126, 54 (2004).
43. J. Yesuraj, V. Elumalai, M. Bhagavathiachari, A.S. Samuel, E. Elaiyappillai, and M. Johnson, *J. Electroanal. Chem.* 797, 78 (2017).
44. M. Daturi, G. Busca, M.M. Borel, F.-C. Cedex, I. Chimica, V. Uni, V. Geno, P.J.F. Kennedy, V. Igeno, C. Industriale, and V. Uni, **5647**, 4358 (1997).
45. S. Saranya, R.K. Selvan, and N. Priyadharsini, *Appl. Surf. Sci.* 258, 4881 (2012).
46. M.N. Iliev, M.M. Gospodinov, and A.P. Litvinchuk, *Phys. Rev. B* 80, 4 (2009).
47. M. Selvamani and U. Polit, *J. Mater. Chem.* 22, 22642 (2016).
48. K. Krishnamoorthy, P. Pazhamalai, G.K. Veerasubramani, and S.J. Kim, *J. Power Sources* 321, 112 (2016).
49. H. Chen, M. Zhou, T. Wang, F. Li, and Y.X. Zhang, *J. Mater. Chem. A* 4, 10786 (2016).
50. F. Xu, R. Cai, Q. Zeng, C. Zou, D. Wu, F. Li, X. Lu, Y. Liang, and R. Fu, *J. Mater. Chem.* 21, 1970 (2011).
51. S. Saranya, S.T. Senthilkumar, K.V. Sankar, and R.K. Selvan, *J. Electroceramics* 28, 220 (2012).
52. J. Tang, J. Shen, N. Li, and M. Ye, *J Alloys Compd.* 666, 15 (2016).
53. H. Kim and B.N. Popov, *J. Electrochem. Soc.* 150, D56 (2003).
54. P. Ragupathy, H.N. Vasan, and N. Munichandraiah, *J. Electrochem. Soc.* 155, A34 (2007).
55. P. Yu, X. Zhang, Y. Chen, and Y. Ma, *Mater. Lett.* 64, 61 (2010).
56. K.H. Chang, C.C. Hu, C.M. Huang, Y.L. Liu, and C.I. Chang, *J. Power Sources* 196, 2387 (2011).
57. N.M. Shinde, A.D. Jagadale, V.S. Kumbhar, T.R. Rana, J.H. Kim, and C.D. Lokhande, *Korean J. Chem. Eng.* 32, 974 (2015).
58. S. Yao, F. Qu, G. Wang, and X. Wu, *J. Alloys Compd.* 724, 695 (2017).
59. K.V. Sankar and R.K. Selvan, *J. Power Sources* 275, 399 (2015).
60. R. Wang, M. Han, Q. Zhao, Z. Ren, X. Guo, C. Xu, N. Hu, and L. Lu, *Sci. Rep.* 7, 44562 (2017).
61. K. Yang, K. Cho, D.S. Yoon, and S. Kim, *Sci. Rep.* 7, 40163 (2017).
62. J. Yesuraj and S.A. Suthanthiraraj, *J. Mol. Struct.* 1181, 131 (2019).
63. J.G. Wang, Y. Yang, Z.H. Huang, and F. Kang, *Carbon N. Y.* 61, 190 (2013).
64. S. Denga, D. Suna, C. Wua, H. Wanga, J. Liua, Y. Suna, and H. Yana, *Electrochim. Acta* 111, 707 (2013).
65. X.W. Wang, D.L. Zheng, P.Z. Yang, X.E. Wang, Q.Q. Zhu, P.F. Ma, and L.Y. Sun, *Chem. Phys. Lett.* 667, 260 (2017).
66. J. Liu, J. Jiang, M. Bosman, and H.J. Fan, *J. Mater. Chem.* 22, 2419 (2012).
67. J. Zhang, Y. Yu, L. Liu, and Y. Wu, *Nanoscale* 5, 3052 (2013).
68. J. Xiao and S. Yang, *J. Mater. Chem.* 22, 12253 (2012).